

Electron collisional excitation cross-section measurements and modeling for select Ni-like to Ge-like gold transitions

M.J. May^a, S.B. Hansen^b, P. Beiersdorfer^a, N.M. Jordan^c, J.H. Scofield^a, K.J. Reed^a, G.V. Brown^a, F.S. Porter^d, R.L. Kelley^d, C.A. Kilbourne^d, and K.R. Boyce^d

^aLawrence Livermore National Laboratory, Livermore, CA 94550, USA; ^bICF Target Design, Sandia National Laboratories, Albuquerque, NM 87185-1186, USA; ^cPlasma Physics, Pulsed Power and Microwave Lab, University of Michigan, Ann Arbor, MI 48109, USA; ^dNASA-Goddard Space Flight Center, Greenbelt, MD 20700, USA

Corresponding author: M.J. May (email: may13@llnl.gov)

Abstract

We have experimentally determined the electron collisional excitation cross-sections for several 3d→4f and 3d→5f excitations in Ni- to Ge-like Au at energies of ~ 0.4, 1, 2, and 3 keV above threshold energy, E_T , for the 3d→4f excitations ($E_T \sim 2.5$ keV) and ~ 0.2, 1, and 2 keV above threshold energy for the 3d→5f excitations ($E_T \sim 3.3$ keV). The cross-section measurements are possible by using the GSFC micro-calorimeter to record emission spectra from beam plasmas created in the Livermore EBIT-I electron beam ion trap. The cross-sections are experimentally determined from the ratio of the measured intensities of the collisionally excited lines to the intensities of the radiative recombination lines in monoenergetic electron distribution EBIT-I plasmas. The effects of polarization and Auger processes in the beam plasmas are accounted for in the cross-section determination. Experimentally determined cross-sections are compared with those from HULLAC, DWS, and FAC calculations. The measurements exhibit significant differences with the calculations of these excitation cross-sections.

Key words: collisional cross-sections, measurement, gold, M-shell, EBIT

1. Introduction

High-temperature plasmas exist in Z-pinch [1, 2], tokamaks [3–5], astrophysical objects [6], and laser-produced plasmas [7–9]. Important parameters, such as radiation output, energy deposition rate, charge state distribution (CSD), etc., must be correctly predicted to understand these plasmas. This is especially true in the complex dynamics of the indirect-driven inertially confined fusion (ICF) plasma experiment [10–12], which depends upon the correct understanding of many physical processes [13]. All these processes must be implemented properly in the ICF modeling codes in order to choose the correct input experimental parameters (e.g. laser drive, hohlraum size, hohlraum material, capsule ablator material, etc.) to optimize the performance of the ICF target.

One of these critical physical processes for ICF is the X-ray radiation drive incident on the D-T fuel capsule from the plasma inside the gold ($Z = 79$) or uranium ($Z = 92$) hohlraum. This radiation drive should result in the compression of the fuel in a very precise and controlled way. The radiation environment inside the hohlraum will have a near-Planckian black body spectrum with radiation temperatures, T_r , of ~300 eV. This quasi-Planckian black body has a significant contribution from non-thermal gold M-shell emission ($E_{\text{photon}} = 2\text{--}4$ keV) [14], which can affect the performance of the fuel cap-

sule. A thorough understanding of the non-local thermodynamic equilibrium (NLTE) gold plasma and radiation environment is needed to optimize the radiation coupling to the ICF target capsule. Failure to predict accurately the gold radiation spectrum can adversely affect the performance of indirectly driven target experiments.

To understand and quantify properly, the X-ray radiation drive from the hohlraum requires detailed knowledge of the underlying atomic structure and atomic processes of the materials composing the ignition hohlraum. There are several key aspects of the atomic physics (e.g. bound-bound transition photon energies, CSDs, line radiation intensities, etc.), which, ideally, need to have a basis in accurate measurements. The results of these measurements are either directly put into the modeling codes or are used to help guide the codes to the correct implementation of the atomic physics.

For instance, one important quantity is the CSD of the gold ions in the plasma. The CSD must be known accurately since it is critical for understanding radiation levels, energy deposition, etc., of the high-temperature plasma at a given condition (electron temperature (T_e), T_r , and electron density (n_e)) [15]. The radiation field surrounding the ICF capsule is dictated by the most abundant ions in the plasma. A shift of a few charge states can significantly alter the energy of the

Table 1. Au $n = 3d \rightarrow 4f$ and $3d \rightarrow 5f$ electron collisional excitations of interest.

Charge State	Iso-sequence	E_T (eV)	E_T (eV)	E_T (eV)	E_T (eV)	$J_{Lower}J_{Upper}$	Collisional excitation
		Measured	HULLAC	FAC	DWS		Transition
Au ⁵¹⁺	Ni-like	2519.8±0.5	2512.84	2509.67	2508.61	0 → 1	$3d^{10} \rightarrow 3d_{3/2}^4 3d_{5/2}^5 4f_{7/2}$
Au ⁵¹⁺	Ni-like	2603.6±0.5	2602.18	2598.34	2600.39	0 → 1	$3d^{10} \rightarrow 3d_{3/2}^3 3d_{5/2}^6 4f_{5/2}$
Au ⁵¹⁺	Ni-like	3370.6±0.5	3370.93	3367.51	3362.27	0 → 1	$3d^{10} \rightarrow 3d_{3/2}^4 3d_{5/2}^5 5f_{7/2}$
Au ⁵¹⁺	Ni-like	3458.3±0.5	3455.86	3452.37	3448.49	0 → 1	$3d^{10} \rightarrow 3d_{3/2}^3 3d_{5/2}^6 5f_{5/2}$
Au ⁵⁰⁺	Cu-like	2501.9±0.5	2496.70	2495.68	2501.60	$\frac{1}{2} \rightarrow \frac{3}{2}$	$3d^{10}4s \rightarrow 3d_{3/2}^4 3d_{5/2}^5 4s4f_{7/2}$
Au ⁵⁰⁺	Cu-like	2589.4±0.5	2586.60	2584.41	2592.99	$\frac{1}{2} \rightarrow \frac{3}{2}$	$3d^{10}4s \rightarrow 3d_{3/2}^3 3d_{5/2}^6 4s4f_{5/2}$
Au ⁵⁰⁺	Cu-like	3334.7±0.5	3334.48	3333.51	3357.84	$\frac{1}{2} \rightarrow \frac{3}{2}$	$3d^{10}4s \rightarrow 3d_{3/2}^4 3d_{5/2}^5 4s5f_{7/2}$
Au ⁵⁰⁺	Cu-like	3420.8±0.5	3419.45	3417.76	3445.64	$\frac{1}{2} \rightarrow \frac{3}{2}$	$3d^{10}4s \rightarrow 3d_{3/2}^3 3d_{5/2}^6 4s5f_{5/2}$
Au ⁴⁹⁺	Zn-like	2480.2±0.5	2485.09	2481.25	2487.10	0 → 1	$3d^{10}4s^2 \rightarrow 3d_{3/2}^4 3d_{5/2}^5 4s^2 4f_{7/2}$
Au ⁴⁹⁺	Zn-like	2572.8±0.5	2574.03	2569.00	2577.50	0 → 1	$3d^{10}4s^2 \rightarrow 3d_{3/2}^3 3d_{5/2}^6 4s^2 4f_{5/2}$
Au ⁴⁹⁺	Zn-like	3296.6±0.5	3302.42	3298.85	3429.80	0 → 1	$3d^{10}4s^2 \rightarrow 3d_{3/2}^4 3d_{5/2}^5 4s^2 5f_{7/2}$
Au ⁴⁹⁺	Zn-like	3382.7±0.5	3387.14	3383.29	3343.30	0 → 1	$3d^{10}4s^2 \rightarrow 3d_{3/2}^3 3d_{5/2}^6 4s^2 5f_{5/2}$
Au ⁴⁸⁺	Ga-like	2469.1±0.5	2469.05	2466.40	2472.10	$\frac{1}{2} \rightarrow \frac{3}{2}$	$3d^{10}4s^2 4p_{1/2} \rightarrow 3d_{3/2}^4 3d_{5/2}^5 4s^2 4p_{1/2} 4f_{7/2}$
Au ⁴⁸⁺	Ga-like	2556.3±0.5	2558.94	2551.98	2560.30	$\frac{1}{2} \rightarrow \frac{3}{2}$	$3d^{10}4s^2 4p_{1/2} \rightarrow 3d_{3/2}^3 3d_{5/2}^6 4s^2 4p_{1/2} 4f_{5/2}$
Au ⁴⁸⁺	Ga-like	3259.9±0.5	3266.31	3263.26	–	$\frac{1}{2} \rightarrow \frac{3}{2}$	$3d^{10}4s^2 4p_{1/2} \rightarrow 3d_{3/2}^4 3d_{5/2}^5 4s^2 4p_{1/2} 5f_{7/2}$
Au ⁴⁸⁺	Ga-like	3348.3±0.5	3351.70	3348.77	–	$\frac{1}{2} \rightarrow \frac{3}{2}$	$3d^{10}4s^2 4p_{1/2} \rightarrow 3d_{3/2}^3 3d_{5/2}^6 4s^2 4p_{1/2} 5f_{5/2}$
Au ⁴⁷⁺	Ge-like	2450.5±0.5	2454.05	2451.31	–	0 → 1	$3d^{10}4s^2 4p_{1/2}^2 \rightarrow 3d_{3/2}^4 3d_{5/2}^5 4s^2 4p_{1/2}^2 4f_{7/2}$
Au ⁴⁷⁺	Ge-like	2539.9±0.5	2541.11	2537.02	–	0 → 1	$3d^{10}4s^2 4p_{1/2}^2 \rightarrow 3d_{3/2}^3 3d_{5/2}^6 4s^2 4p_{1/2}^2 4f_{5/2}$
Au ⁴⁷⁺	Ge-like	3226.5±0.5	3230.99	3227.96	–	0 → 1	$3d^{10}4s^2 4p_{1/2}^2 \rightarrow 3d_{3/2}^4 3d_{5/2}^5 4s^2 4p_{1/2}^2 5f_{7/2}$
Au ⁴⁷⁺	Ge-like	3312.2±0.6	3316.56	3312.95	–	0 → 1	$3d^{10}4s^2 4p_{1/2}^2 \rightarrow 3d_{3/2}^3 3d_{5/2}^6 4s^2 4p_{1/2}^2 5f_{5/2}$

radiation field. The energy deposited in the ICF capsule ablator directly affects the dynamics of the implosion.

Accurate electron collisional excitation cross-sections are needed since these rates are used for proper interpretation of the spectral intensities of highly charged gold ions for plasma diagnostics. In fact, the determination of the ionization balance for a given plasma temperature is especially sensitive to the values of the excitation cross-sections used to correlate the intensity of a given line to the abundance of the emitting ion species. Also, the intensity of the emission lines directly affects the total strength of the radiation field. Since inaccuracies in the calculated cross-sections affect the understanding of the plasma, understanding their accuracy and uncertainty is important. Accurate measurements of the cross-sections will reduce these uncertainties.

To this end, we present our measurements and discuss our technique for measuring the electron collisional excitation cross-sections of selected M-shell transitions in Ni- to Ge-like Au that contribute to the non-thermal component of the ICF hohlraum radiation drive. Details of the $3d_{3/2} \rightarrow 4f_{5/2}$, $3d_{5/2} \rightarrow 4f_{7/2}$, $3d_{3/2} \rightarrow 5f_{5/2}$, and $3d_{5/2} \rightarrow 5f_{7/2}$ excitations cross-sections investigated in this paper are given in Table 1. The measurements were done at the Livermore EBIT-I electron beam ion trap [16, 17], which has unique capabilities that allow the measurement of excitation cross-sections of highly charged ions, as detailed by Chen et al. [18]. The cross-sections were determined by fitting the observed $4f \rightarrow 3d$ and $5f \rightarrow 3d$ line emission and normalizing this emission to the recorded radiative recombination (RR) emission from the same ion and in the same plasma. The experimentally determined cross-sections are compared with the calculated

cross-sections from the Hebrew University-Lawrence Livermore Atomic Code (HULLAC) [19], the Distorted Wave Code (DWS) [20], and the Flexible Atomic Code (FAC) [21, 22].

2. Plasmas at the Livermore electron beam ion trap

The gold plasmas for the collisional excitation cross-section measurements were created in the Livermore EBIT-I electron beam ion trap. Two different types of trapping cycles having either a single monoenergetic beam energy condition or a stepped-in-time two beam energy condition were used to create the appropriate plasma conditions for these measurements. The plasma conditions are detailed in Table 2. The different conditions were chosen to measure the collisional excitation cross-sections at several energies above the excitation threshold energy, E_T , for each transition. The measured E_T are given in Table 1 with uncertainties. The E_T calculated by HULLAC, FAC, and DWS are also given and differ from the measured values by 1 to 5 eV.

Several conditions were chosen having single beam energies, E_{Beam} (e.g. 2.92, 3.53, and 4.54 ± 0.04 keV). For these conditions, the beam energy was kept constant for the duration of the trapping cycle. The stepped two beam energy plasmas had a lower energy (e.g. $E_{Beam} = 2.92 \pm 0.04$ keV) for 43 ms followed by a higher energy (e.g. $E_{Beam} = 5.35 \pm 0.04$ keV) for 7 ms before immediately returning to the lower energy. This step pattern was repeated for the duration of each trapping cycle. In the stepped plasmas, the lower beam energy plasma conditions were used to create the required charge balance and to optimize the population of the ions of interest. The

Table 2. Electron beam energy configurations utilized for the electron collisional excitation cross-section measurements.

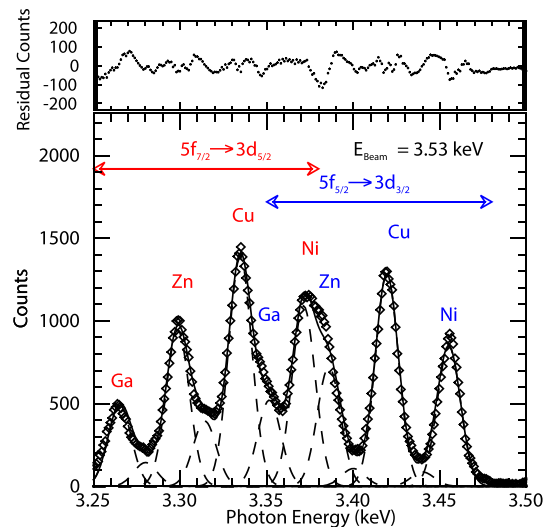
Dominant Ions	Lower E_{Beam} (keV)	Upper E_{Beam} (keV)	I_{Beam} (mA)	Duration of lower E_{Beam} (ms)	Duration of higher E_{Beam} (ms)
Ni/Cu/Zn	5.35 ± 0.04	—	56	—	—
Ni/Cu/Zn	4.54 ± 0.04	—	56	—	—
Ni/Cu/Zn	3.53 ± 0.04	—	56	—	—
Zn/Ga/Ge	2.92 ± 0.04	—	50	—	—
Zn/Ga/Ge	2.92 ± 0.04	3.53 ± 0.04	50	43	7
Zn/Ga/Ge	2.92 ± 0.04	4.54 ± 0.04	50	43	7
Zn/Ga/Ge	2.92 ± 0.04	5.35 ± 0.04	54	43	7
Ni/Cu/Zn	4.54 ± 0.04	5.35 ± 0.04	56	43	7

higher beam energy conditions were used to create electrons of the required energy. These electrons excited the ions in the $3d^n$ ground state into either the upper $4f$ or $5f$ transition with a specific E_T of the collisional excitation. In the single beam energy plasmas, both the charge balance and electron excitation conditions were satisfied using a single beam energy. The electron beam for these experiments had a Gaussian electron energy distribution with a full width half maximum (FWHM) of ≈ 50 eV. Each of these trapping cycle conditions having either a single or stepped two beam energy plasma was maintained for 8 to 12 s before the trap was emptied and refilled with new Au atoms. The trapping cycle at each experimental condition was repeated for ≈ 12 h in order to record sufficient signal in the weak RR emission.

The Goddard Space Flight Center (GSFC) microcalorimeter (XRS) [23, 24] was photometrically calibrated and was used to record the collisionally excited Ni- to Ge-like gold lines from the $4f \rightarrow 3d$ and $5f \rightarrow 3d$ X-ray transitions between photon energies, E_γ , of 2 to 4 keV and the RR features of Ni recombining into Cu, Cu recombining into Zn, etc., between E_γ of 5 and 8 keV. The XRS detector head consisted of an array of 30 active ion-implanted thermistors with a $8.5 \mu\text{m}$ thick HgTe photon absorber. The thermistors directly measured the temperature change of a single photon absorbed by the HgTe absorber, which was cooled to 59 mK. The maximum count rate was limited to ≈ 100 counts per second across the entire array. The spectral resolution was ≈ 12 eV across the entire spectral range used for these measurements. This resolution was slightly poorer than the 10 eV nominal resolution of other XRS measurements [25, 26] and may be the result of small instrumental drifts during the 12 h integration times.

The XRS was time synchronized with the EBIT-I trapping cycle. Each photon had a time stamp relating its detection time to the time of the trapping cycle. Only the steady state portion of each single beam energy plasma condition was selected, and this spectrum was used for these measurements. For the stepped two electron beam energy conditions, the steady state portions of each beam condition were selected. The RR spectrum from the lower energy condition and collisionally excited spectrum from the upper energy conditions were used for the collisional excitation cross-section measurements.

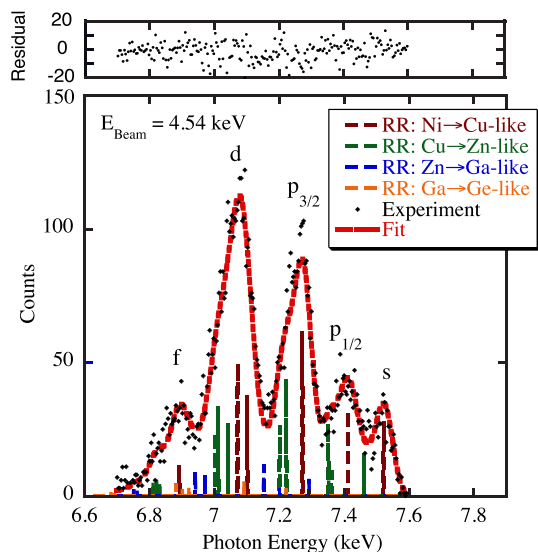
Fig. 1. Measured microcalorimeter (XRS) [23, 24] spectrum of the $n=5f \rightarrow 3d$ Au transitions in an EBIT-I plasma having an E_{Beam} of 3.53 keV. The lower panel shows the spectrum (dots) and the fit to the data. The dashed lines are the components to the total fit (solid line). The upper panel shows the residual of the fit to the data indicating the goodness of the fit.



A typical measured line emission spectrum (dots) of M-shell gold between $E_\gamma = 3.2\text{--}3.6$ keV is given in the lower frame of Fig. 1. An E_{Beam} of 3.53 keV was used to create the Ni-, Cu- and Zn-like Au charge states that are the dominant charge states at this beam energy. Clearly seen are the $n = 5f_{7/2} \rightarrow 3d_{5/2}$ and $n = 5f_{5/2} \rightarrow 3d_{3/2}$ transitions of interest. Fits to the data are discussed below.

A typical measured RR spectrum (dots) is shown for an Au plasma having an $E_{\text{Beam}} = 4.54$ keV, in the lower frame of Fig. 2. The measured recombination features from the continuum into the $n = 4s, 4p_{1/2}, 4p_{3/2}, 4d,$ and $4f$ sublevels are observed and are labeled in the figure. The major contributing charge states to these feature are the Ni-like ions recombining into Cu-like ions, Cu-like ions recombining into Zn-like ions, and Zn-like ions recombining into Ga-like gold ions. Additional spectra and details of the EBIT measurements are given in Refs. [27–30].

Fig. 2. A radiative recombination (RR) spectrum from an Au plasma with an E_{Beam} of 4.54 keV measured by the XRS. In the lower panel, the RR features are fit with calculations from GRASP. The upper panel shows the residual of the fit to the data indicating the goodness of the fit.



3. Cross-section calculations

Since atomic physics codes can calculate electron collisional excitation cross-sections with slightly different methods, a comparison of the computational methods of several codes is prudent. Three separate atomic physics codes (HULLAC [19], DWS [20] and FAC [21, 22]) were used to calculate the electron collisional excitation cross-sections for the $3d \rightarrow 4f$ and $3d \rightarrow 5f$ excitations discussed here. HULLAC computed the energy-level structure for each ion from the Dirac equation with a parametric potential. Total electron collisional excitation cross-sections were calculated semi-relativistically in the distorted wave approximation. DWS calculated fully relativistic distorted wave cross-sections and utilized the Dirac-Fock-Slater potential. FAC calculated cross-sections in the distorted wave approximation using the same factorization formula used by HULLAC and a variant of the potential used by DWS. HULLAC can only calculate the total cross-sections. The FAC and DWS codes can calculate the cross-sections between the individual magnetic sub-levels that are important for processes driven by a highly directional beam such as in EBIT. The configurations used for each of the calculations are listed in Table 3. The configurations used by FAC and HULLAC differed slightly. The DWS configurations were minimal due to the complexities of running this code. All the calculations utilized the configuration-interaction (CI) method. The calculated excitation cross-sections from HULLAC, FAC, and DWS for the transitions in Ni- to Ge-like gold are given in Tables 4, 5, and 6. The cross-sections calculated by the three codes are compared in Figs. 3, 4, 5, 6, and 7 for Ni-, Cu-, Zn-, Ga- and Ge-like gold, respectively. In general, the agreement between the total cross-sections calculated by all three codes was good. The variations between the differ-

ent calculations were 10%–20%. The magnetic sub-level cross-sections from FAC were in good agreement with those from DWS. In a recent paper, Wu *et al.* [31] have calculated both cross-sections and polarizations, P , of the $3d \rightarrow 5f$ lines for Cu-like to Se-like gold following electron-impact excitation. These calculated cross-sections for Cu-like gold are plotted in Fig. 4 and are in reasonable agreement with the three calculations presented here.

4. Collisional excitation cross-section measurements

The experimentally inferred collisional excitation cross-sections for the $3d \rightarrow 4f$ and $3d \rightarrow 5f$ excitations in Ni-like to Ge-like gold were determined from the measured intensities of the collisionally excited lines, I_{CE} , and the RR emission, I_{RR} . These cross-sections, σ_{CE} , are related to the I_{CE} and I_{RR} intensities by the formula:

$$\sigma_{\text{CE}} = \frac{1}{\beta_{\text{AA}}} \frac{\sum_j G_{\text{RR},j} \eta_{\text{RR},j} T_{\text{RR},j} \sigma_{\text{RR},j} I_{\text{CE}}}{G_{\text{CE}} \eta_{\text{CE}} T_{\text{CE}} I_{\text{RR}}} \quad (1)$$

The variables η and T are the XRS detector efficiency and filter transmissions in the XRS, respectively. The variable β_{AA} is the branching ratio that accounts for the autoionization processes that affect each transition. The values $\sigma_{\text{RR},j}$ are the RR cross-sections. G_{CE} and $G_{\text{RR},j}$ are the corrections for the polarization effects on the measured I_{CE} and I_{RR} intensities, respectively. In the single beam energy plasmas, the I_{CE} and I_{RR} data used were fits of the spectra recorded from the steady state portion in each beam configuration. In the stepped two beam energy plasmas, the I_{CE} line data were fits of the spectrum recorded in the steady state portion of the upper beam energy condition in a given configuration. Similarly, the I_{RR} emission data were fits of the spectrum recorded in the steady state portion of the lower beam energy condition in a given configuration. These intensities were corrected for the different time durations spent at each beam energy condition during the trapping cycle.

We note that two types of polarizations can influence these cross-section measurements. The first is due to the measurement detection technique. Some X-ray measurement techniques (e.g. using crystals) are selective in the detection of different polarizations [32]. These techniques change the polarization of the detected photons and require additional corrections for a cross-section determination. However, the XRS detector records all photons equally regardless of polarization. No detector correction for polarization is required for the XRS-recorded spectra.

The second polarization is that from geometry and the viewing angle of the measurement. Both the line and RR emission from the EBIT-I plasmas are polarized as a result of the ions undergoing electron excitations in a directional electron beam. The intensity and polarization of a given emission feature from a beam-excited ion depends on the observation angle relative to the direction defined by the relative velocities of the ion and the electron. In the EBIT plasmas, we assume that the ions are quasi-stationary and are interacting

Table 3. Atomic configurations used for FAC, HULLAC, and DWS calculations.

FAC Ni-like	HULLAC Ni-like	DWS Ni-like
1s2 2[s,p]8 3[s,p,d]18	1s2 2[s,p]8 3p6 3d10	1s2 2[s,p]8 3p6 3d10
1s2 2[s,p]8 3s2 3p6 3d8 4s1 4[p,d,f]1	1s2 2[s,p]8 3p6 3d9 4[s,p,d,f]1	1s2 2[s,p]8 3p6 3d9 4[p,f]1
1s2 2[s,p]8 3s2 3p6 3d8 4s2	1s2 2[s,p]8 3p6 3d9 5[s,p,d,f]1	1s2 2[s,p]8 3p6 3d9 5[p,f]1
1s2 2[s,p]8 3s2 3p6 3d8 4s1 5f1	1s2 2[s,p]8 3p5 3d10 4[s,p,d,f]1	
1s2 2[s,p]8 3[s,p,d]17 4[s,p,d,f]1	1s2 2[s,p]8 3p5 3d10 5[s,p,d,f]1	
1s2 2[s,p]8 3[s,p,d]17 5[s,p,d,f,g]1		
1s2 2[s,p]8 3[s,p,d]17 6[s,p,d,f,g]1		
1s2 2[s,p]7 3s2 3p6 3d10 4[s,p,d,f]1		
1s1 2[s,p]8 3s2 3p6 3d10 4[s,p,d,f]1		
FAC Cu-like	HULLAC Cu-like	DWS Cu-like
1s2 2[s,p]8 3[s,p,d]18 4s1	1s2 2[s,p]8 3p6 3d10 4[s,p,d,f]1	1s2 2[s,p]8 3p6 3d10 4s1
1s2 2[s,p]8 3[s,p,d]18 4[s,p,d,f]1	1s2 2[s,p]8 3p6 3d10 4[s,p,d,f]1	1s2 2[s,p]8 3p6 3d9 4s1 4[p,f]1
1s2 2[s,p]8 3[s,p,d]18 5[s,p,d,f,g]1	1s2 2[s,p]8 3p6 3d9 4s1 4[s,p,d,f]1	1s2 2[s,p]8 3p6 3d9 4s1 5[p,f]1
1s2 2[s,p]8 3[s,p,d]18 6[s,p,d,f,g]1	1s2 2[s,p]8 3p6 3d9 4s1 5[s,p,d,f]1	
1s2 2[s,p]8 3[s,p,d]17 4s2	1s2 2[s,p]8 3p5 3d10 4s1 4[s,p,d,f]1	
1s2 2[s,p]8 3[s,p,d]17 4s1 4[p,d,f]1	1s2 2[s,p]8 3p5 3d10 4s1 5[s,p,d,f]1	
1s2 2[s,p]8 3[s,p,d]17 4s1 5[s,p,d,f]1		
FAC Zn-like	HULLAC Zn-like	DWS Zn-like
1s2 2[s,p]8 3[s,p,d]18 4s2	1s2 2[s,p]8 3p6 3d10 4[s,p,d,f]2	1s2 2[s,p]8 3p6 3d10 4s2
1s2 2[s,p]8 3[s,p,d]18 4s1 4[p,d,f]1	1s2 2[s,p]8 3p6 3d10 4s1 5[s,p,d,f]1	1s2 2[s,p]8 3p6 3d9 4s2 4[p,f]1
1s2 2[s,p]8 3[s,p,d]18 4s1 5[s,p,d,f,g]1	1s2 2[s,p]8 3p6 3d9 4s2 4[p,d,f]1	1s2 2[s,p]8 3p6 3d9 4s2 5[p,f]1
1s2 2[s,p]8 3[s,p,d]18 4s1 6[s,p,d,f,g]1	1s2 2[s,p]8 3p6 3d9 4s2 5[s,p,d,f]1	
1s2 2[s,p]8 3[s,p,d]17 4s2 4[p,d,f]1	1s2 2[s,p]8 3p5 3d10 4s2 4[p,d,f]1	
1s2 2[s,p]8 3[s,p,d]17 4s2 5[s,p,d,f,g]1	1s2 2[s,p]8 3p5 3d10 4s2 5[s,p,d,f]1	
FAC Ga-like	FAC Ga-like	DWS Ga-like
1s2 2[s,p]8 3[s,p,d]18 4s2 4p1	1s2 2[s,p]8 3p6 3d10 4s2 4[p,d,f]1	1s2 2[s,p]8 3p6 3d10 4s3
1s2 2[s,p]8 3[s,p,d]18 4s2 4[d,f]1	1s2 2[s,p]8 3p6 3d10 4s2 5[s,p,d,f]1	1s2 2[s,p]8 3p6 3d9 4s2 4[p,f]1
1s2 2[s,p]8 3[s,p,d]18 4s1 4p2	1s2 2[s,p]8 3p6 3d10 4s1 4[p,d,f]2	
1s2 2[s,p]8 3[s,p,d]18 4s1 4p1 4[d,f]1	1s2 2[s,p]8 3p6 3d10 4p1 4[d,f]2	
1s2 2[s,p]8 3[s,p,d]18 4s2 5[s,p,d,f,g]1	1s2 2[s,p]8 3p6 3d10 4d1 4f2	
1s2 2[s,p]8 3[s,p,d]18 4s2 6[s,p,d,f,g]1	1s2 2[s,p]8 3p6 3d10 4d2 4f1	
1s2 2[s,p]8 3s2 3p6 3d9 4s2 4p2	1s2 2[s,p]8 3p6 3d10 4s1 4p1 5[s,p,d,f]1	
1s2 2[s,p]8 3s2 3p6 3d9 4s2 4p1 4f1	1s2 2[s,p]8 3p6 3d9 4s2 4p1 5[s,p,d,f]1	
1s2 2[s,p]8 3s2 3p6 3d9 4s2 4p1 5f1	1s2 2[s,p]8 3p6 3d9 4s2 4p1 4[p,d,f]1	
	1s2 2[s,p]8 3p5 3d10 4s2 4p1 5[s,p,d,f]1	
	1s2 2[s,p]8 3p5 3d10 4s2 4p1 4[p,d,f]1	
FAC Ge-like	FAC Ge-like	DWS Ge-like
1s2 2[s,p]8 3[s,p,d]18 4s2 4p2	1s2 2[s,p]8 3p6 3d10 4s2 4[p,d,f]2	Not available
1s2 2[s,p]8 3[s,p,d]18 4s2 4p1 4[d,f]1	1s2 2[s,p]8 3p6 3d10 4s2 4p1 5[s,p,d,f]1	
1s2 2[s,p]8 3[s,p,d]18 4s1 4p3	1s2 2[s,p]8 3p6 3d10 4s1 4p2 4[p,d,f]1	
1s2 2[s,p]8 3[s,p,d]18 4s1 4p2 4[d,f]1	1s2 2[s,p]8 3p6 3d10 4s1 4p2 5[s,p,d,f]1	
1s2 2[s,p]8 3[s,p,d]18 4s2 4p1 5[s,p,d,f,g]1		
1s2 2[s,p]8 3[s,p,d]18 4s2 4p1 6[s,p,d,f,g]1		
1s2 2[s,p]8 3s2 3p6 3d9 4s2 4p3		
1s2 2[s,p]8 3s2 3p6 3d9 4s2 4p2 4f1		
1s2 2[s,p]8 3s2 3p6 3d9 4s2 4p2 5f1		

with electrons traveling along a single beam direction. In this work, the emission is viewed 90° from the direction of the electron beam. Corrections for the polarization are applied to the measured RR and the CE emission for more accurate de-

terminations of each of the cross-sections. These corrections are included by different methods as detailed below.

The General Relativistic Atomic Structure Program (GRASP) [33, 34] provided RR cross-sections, $\sigma_{RR,j}$, that

Table 4. Selected collisional excitation cross-sections of interest from HULLAC.

Iso sequence	Transition (J-J)	Energy Above Threshold (eV)	$3d_{5/2} \rightarrow 4f_{7/2}$ $\sigma (\times 10^{-21})$ (cm ²)	$3d_{3/2} \rightarrow 4f_{5/2}$ $\sigma (\times 10^{-21})$ (cm ²)	$3d_{5/2} \rightarrow 5f_{7/2}$ $\sigma (\times 10^{-21})$ (cm ²)	$3d_{3/2} \rightarrow 5f_{5/2}$ $\sigma (\times 10^{-21})$ (cm ²)
Photon energy (eV)			2512.84	2602.18	3370.93	3455.86
Ni-like	A (s ⁻¹)		2.114×10^{14}	5.460×10^{14}	1.684×10^{14}	2.006×10^{14}
Ni-like	0→1	100	17.250	37.780	5.391	5.593
Ni-like	0→1	1000	14.840	32.950	4.782	5.081
Ni-like	0→1	2000	13.320	29.440	4.357	4.654
Ni-like	0→1	5000	10.420	23.560	3.529	3.821
Ni-like	0→1	10000	8.021	18.280	2.780	3.020
Ni-like	0→1	20000	5.957	13.640	2.065	2.254
Photon energy (eV)			2496.80	2586.76	3333.71	3419.38
Cu-like	A (s ⁻¹)		2.124×10^{14}	5.278×10^{14}	1.658×10^{14}	1.922×10^{14}
Cu-like	1/2→3/2	100	11.500	24.120	3.338	4.387
Cu-like	1/2→3/2	1000	9.928	21.090	2.991	3.820
Cu-like	1/2→3/2	2000	8.809	18.860	2.795	2.927
Cu-like	1/2→3/2	5000	6.935	15.000	2.267	2.396
Cu-like	1/2→3/2	10000	5.410	11.790	1.788	1.904
Cu-like	1/2→3/2	20000	4.021	8.808	1.328	1.422
Photon energy (eV)			2485.09	2574.03	3302.42	3387.14
Zn-like	A (s ⁻¹)		2.133×10^{14}	5.353×10^{14}	1.673×10^{14}	1.954×10^{14}
Zn-like	0→1	100	15.740	39.570	5.667	5.322
Zn-like	0→1	1000	14.730	31.760	4.808	4.846
Zn-like	0→1	2000	13.080	28.440	4.389	4.446
Zn-like	0→1	5000	10.320	22.680	3.567	3.642
Zn-like	0→1	10000	8.061	17.850	2.821	2.895
Zn-like	0→1	20000	6.000	13.340	2.096	2.162
Photon energy (eV)			2469.05	2555.78	3265.88	3351.70
Ga-like	A (s ⁻¹)		2.075×10^{14}	5.325×10^{14}	1.671×10^{14}	1.944×10^{14}
Ga-like	1/2→3/2	100	11.390	24.530	3.647	1.853
Ga-like	1/2→3/2	1000	10.830	23.730	3.531	1.813
Ga-like	1/2→3/2	2000	9.721	21.530	3.257	1.689
Ga-like	1/2→3/2	5000	7.906	17.720	2.754	1.441
Ga-like	1/2→3/2	10000	5.353	12.190	1.915	1.012
Ga-like	1/2→3/2	20000	3.302	7.579	1.182	0.630
Photon energy (eV)			2454.05	2541.11	3230.99	3316.56
Ge-like	A (s ⁻¹)		2.088×10^{14}	5.120×10^{14}	1.673×10^{14}	1.967×10^{14}
Ge-like	0→1	100	16.890	35.540	5.632	5.829
Ge-like	0→1	1000	14.630	31.240	5.075	5.316
Ge-like	0→1	2000	13.020	28.060	3.762	4.880
Ge-like	0→1	5000	10.280	22.440	3.762	4.004
Ge-like	0→1	10000	8.046	17.710	2.972	3.187
Ge-like	0→1	20000	5.994	13.260	2.208	2.383

included the polarization effects, $G_{RR,j}$, in the EBIT-I plasmas. These calculated features were fit to the measured spectra to determine the I_{RR} for each beam condition. In the beam plasma, the RR features appear as lines with widths equal to FWHM of the Gaussian electron energy distribution of ≈ 50 eV. The energy of the 'line' is equal to the beam energy plus the energy of recombination from the continuum into the recombined state. Each RR feature was assumed to have a

Gaussian energy distribution which was used in the fitting process. An example fit (red dashed line) of these features to the measured spectra is given in the lower frame of Fig. 2 for an $E_{beam} = 4.54$ keV plasma condition. The individual RR features are given as vertical lines in the figure. The upper frame in Fig. 2 shows the small residual between the measured data and the fit, which indicates the quality of the fit.

Table 5. Selected polarizations and collisional excitation cross sections of interest from FAC.

Iso sequence	Transition (J-J)	Energy above Threshold (eV)	$3d_{5/2} \rightarrow 4f_{7/2}$			$3d_{3/2} \rightarrow 4f_{5/2}$			$3d_{5/2} \rightarrow 5f_{7/2}$			$3d_{3/2} \rightarrow 5f_{5/2}$		
			P	G	$\sigma (\times 10^{-21})$ (cm ²)	P	G	$\sigma (\times 10^{-21})$ (cm ²)	P	G	$\sigma (\times 10^{-21})$ (cm ²)	P	G	$\sigma (\times 10^{-21})$ (cm ²)
Photon energy (eV)			2509.67			2598.34			3367.51			3452.37		
Ni-like	A (s ⁻¹)		2.124×10^{14}			5.377×10^{14}			1.598×10^{14}			1.832×10^{14}		
Ni-like	0→1	148.07	0.286	1.11	16.907	0.285	1.10	36.251	0.278	1.10	5.004	0.278	1.10	5.047
Ni-like	0→1	2088.2	0.369	1.14	12.891	0.369	1.14	28.231	0.353	1.13	4.123	0.355	1.13	4.206
Ni-like	0→1	5073.9	0.378	1.14	10.181	0.380	1.15	22.548	0.371	1.14	3.370	0.375	1.14	3.467
Ni-like	0→1	9668.4	0.325	1.12	8.061	0.329	1.12	17.969	0.329	1.12	2.701	0.336	1.13	2.796
Ni-like	0→1	16739	0.231	1.08	6.437	0.237	1.09	14.404	0.248	1.09	2.150	0.257	1.09	2.235
Ni-like	0→1	27619	0.102	1.04	4.575	0.109	1.04	10.235	0.108	1.04	1.535	0.118	1.04	1.596
Photon energy (eV)			2495.68			2584.41			3333.51			3417.76		
Cu-like	A (s ⁻¹)		2.108×10^{14}			5.123×10^{14}			1.561×10^{14}			1.746×10^{14}		
Cu-like	1/2→3/2	146.83	0.149	1.05	11.290	0.146	1.05	23.238	0.140	1.05	3.338	0.145	1.05	3.284
Cu-like	1/2→3/2	2067.7	0.196	1.07	8.661	0.195	1.07	18.197	0.185	1.07	2.762	0.188	1.07	2.748
Cu-like	1/2→3/2	5023.7	0.202	1.07	6.863	0.203	1.07	14.579	0.197	1.07	2.264	0.201	1.07	2.271
Cu-like	1/2→3/2	9572.5	0.173	1.06	5.447	0.175	1.06	11.645	0.174	1.06	1.817	0.179	1.06	1.835
Cu-like	1/2→3/2	16572.	0.121	1.04	4.354	0.124	1.04	9.345	0.130	1.05	1.449	0.135	1.05	1.468
Cu-like	1/2→3/2	27344.	0.052	1.02	3.099	0.056	1.02	6.652	0.056	1.02	1.036	0.061	1.02	1.050
Photon energy (eV)			2481.25			2569.00			3298.85			3383.29		
Zn-like	A (s ⁻¹)		2.084×10^{14}			5.111×10^{14}			1.530×10^{14}			1.717×10^{14}		
Zn-like	0→1	145.65	0.280	1.10	16.933	0.278	1.10	35.151	0.272	1.10	5.033	0.272	1.10	4.964
Zn-like	0→1	2047.1	0.367	1.14	13.052	0.367	1.14	27.680	0.352	1.13	4.181	0.353	1.13	4.170
Zn-like	0→1	4973.1	0.379	1.14	10.375	0.380	1.15	22.251	0.372	1.14	3.435	0.376	1.14	3.455
Zn-like	0→1	9475.7	0.328	1.12	8.249	0.331	1.12	17.805	0.332	1.12	2.763	0.338	1.13	2.796
Zn-like	0→1	16404.	0.234	1.08	6.604	0.240	1.09	14.311	0.251	1.09	2.205	0.260	1.09	2.241
Zn-like	0→1	27066.	0.105	1.04	4.710	0.112	1.04	10.205	0.111	1.04	1.580	0.121	1.04	1.606
Photon energy (eV)			2466.40			2551.98			3263.26			3348.77		
Ga-like	A (s ⁻¹)		2.003×10^{14}			5.023×10^{14}			1.499×10^{14}			1.593×10^{14}		
Ga-like	1/2→3/2	144.44	0.146	1.05	10.964	0.145	1.05	23.214	0.142	1.05	3.366	0.134	1.05	3.153
Ga-like	1/2→3/2	2105.8	0.196	1.07	8.429	0.196	1.07	18.273	0.188	1.07	2.792	0.184	1.07	2.643
Ga-like	1/2→3/2	5125.0	0.202	1.07	6.692	0.204	1.07	14.692	0.199	1.07	2.289	0.199	1.07	2.183
Ga-like	1/2→3/2	9772.6	0.172	1.06	5.316	0.175	1.06	11.752	0.175	1.06	1.836	0.177	1.06	1.762
Ga-like	1/2→3/2	16927.	0.118	1.04	4.255	0.123	1.04	9.444	0.128	1.04	1.465	0.132	1.05	1.411
Ga-like	1/2→3/2	27939.	0.050	1.02	3.027	0.055	1.02	6.723	0.053	1.02	1.047	0.057	1.02	1.009

Table 5. (concluded).

Iso sequence	Transition (J-J')	Energy above Threshold (eV)	3d _{5/2} → 4f _{7/2}			3d _{3/2} → 4f _{5/2}			3d _{5/2} → 5f _{7/2}			3d _{3/2} → 5f _{5/2}		
			P	G	σ (×10 ⁻²¹) (cm ²)	P	G	σ (×10 ⁻²¹) (cm ²)	P	G	σ (×10 ⁻²¹) (cm ²)	P	G	σ (×10 ⁻²¹) (cm ²)
Ge-like	0 → 1	143.25	0.275	1.10	16.556	0.273	1.10	33.770	0.264	1.10	5.067	0.266	1.10	4.855
Ge-like	0 → 1	2164.9	0.368	1.14	12.701	0.369	1.14	26.542	0.354	1.13	4.192	0.354	1.13	4.064
Ge-like	0 → 1	5277.8	0.377	1.14	10.072	0.381	1.15	21.314	0.372	1.14	3.429	0.376	1.14	3.350
Ge-like	0 → 1	10071.	0.320	1.12	7.996	0.327	1.12	17.036	0.327	1.12	2.744	0.331	1.12	2.698
Ge-like	0 → 1	17452.	0.220	1.08	6.414	0.230	1.08	13.711	0.239	1.09	2.188	0.247	1.09	2.160
Ge-like	0 → 1	28816.	0.091	1.03	4.541	0.100	1.03	9.719	0.096	1.03	1.561	0.104	1.04	1.539
Photon energy (eV)			2451.31			2537.02			3227.96			3312.95		
A (s ⁻¹)			1.998 × 10 ¹⁴			4.833 × 10 ¹⁴			1.466 × 10 ¹⁴			1.597 × 10 ¹⁴		

For each line emission spectrum, each line feature is fit with a Gaussian line function to determine the I_{CE} of each transition. An example of a fit is given in the lower frame of Fig. 1 for the $5f_{5/2} \rightarrow 3d_{3/2}$ and $5f_{7/2} \rightarrow 3d_{5/2}$ emission lines for a plasma having an $E_{beam} = 3.53$ keV. The individual Gaussian fits are shown as dashed lines with a nominal FWHM of the instrumental spectral resolution of ≈ 12 eV. The total fit (solid line), which is the sum of the dashed Gaussian peaks, compares well with the measured spectrum. The upper frame in Fig. 1 shows the residual between the measured data and the fit. The residual is small indicating a good fit to the data and an accurate determination of the intensity of each spectral line.

For I_{CE} emission, the polarization at an observation angle of $\theta = 90^\circ$ with respect to the electron beam can be expressed as follows:

$$P = \frac{I_{\parallel} - I_{\perp}}{I_{\parallel} + I_{\perp}} \tag{2}$$

I_{\parallel} and I_{\perp} are the intensities of light with electric field vector parallel and perpendicular to the electron beam direction, respectively [35]. The polarization can be expressed as a function of the magnetic sublevel cross-sections, which is discussed in more detail in Ref. [36]. The magnetic sublevel cross-sections were calculated by DWS and FAC. For the Ni-like, Zn-like and, Ge-like $4f_{5/2} \rightarrow 3d_{3/2}$, $4f_{7/2} \rightarrow 3d_{5/2}$, $5f_{5/2} \rightarrow 3d_{3/2}$, and $5f_{7/2} \rightarrow 3d_{5/2}$ transitions that have $J = 1 \rightarrow 0$ [36]:

$$P = -1 \times \frac{\sigma_{-1} - 2\sigma_0 + \sigma_{+1}}{\sigma_{-1} + 2\sigma_0 + \sigma_{+1}} \tag{3}$$

For the Cu-like and Ga-like $4f_{5/2} \rightarrow 3d_{3/2}$, $4f_{7/2} \rightarrow 3d_{5/2}$, $5f_{5/2} \rightarrow 3d_{3/2}$ and $5f_{7/2} \rightarrow 3d_{5/2}$ transitions having $J = \frac{3}{2} \rightarrow \frac{1}{2}$ [36]:

$$P = \frac{3(\sigma_{\frac{1}{2}} - \sigma_{\frac{3}{2}})}{3\sigma_{\frac{3}{2}} + 5\sigma_{\frac{1}{2}}} \tag{4}$$

Each of the magnetic sub-level cross-sections has an implicit energy dependence. Therefore, the polarization of an emitted photon varies with beam energy. The polarizations for the $4f \rightarrow 3d$ and $5f \rightarrow 3d$ Cu-like (Au^{51+}) and Zn-like (Au^{50+}) transitions determined using the calculated cross-sections from both DWS and FAC are plotted in Figs. 8 and 9, respectively, as a function of E_T . The calculated polarizations of the $3d \rightarrow 5f$ lines for Cu-like gold from Wu *et al.* [31] are also plotted in Fig. 8. Reasonable agreement exists between the calculations of Wu *et al.* and the calculations presented here for the Cu-, Zn-, Ga- and Ge-like polarizations. The polarizations determined from both FAC and DWS are in good agreement. The polarizations have a maximum at about 5 keV above E_T . The polarizations used for the transitions are given in Table 5 as determined from the FAC calculations. The polarization is ≈ 0.35 at a $E_{beam} = 4.54$ keV for the $4f \rightarrow 3d$ ($J = 1 \rightarrow 0$) and $5f \rightarrow 3d$ ($J = 1 \rightarrow 0$) transitions in Zn-like Au. The polarization is ≈ 0.2 for this beam energy for the transitions having $J = \frac{3}{2} \rightarrow \frac{1}{2}$ in Cu-like gold. Because of the high-electron beam energy of the present measurements, depolarization effects caused by

Table 6. Selected collisional excitation cross-sections of interest from DWS.

Iso sequence	Transition (J-J)	Energy above threshold (eV)	$3d_{5/2} \rightarrow 4f_{7/2}$ $\sigma (\times 10^{-21})$ (cm ²)	Energy above threshold (eV)	$3d_{3/2} \rightarrow 4f_{5/2}$ $\sigma (\times 10^{-21})$ (cm ²)	Energy above threshold (eV)	$3d_{5/2} \rightarrow 5f_{7/2}$ $\sigma (\times 10^{-21})$ (cm ²)	Energy above Threshold (eV)	$3d_{3/2} \rightarrow 5f_{5/2}$ $\sigma (\times 10^{-21})$ (cm ²)
Ni-like	Photon energy (eV)	2508.61		2600.39		3362.27		3448.49	
Ni-like	0→1	–	–	–	–	190.0	4.916	110.0	4.907
Ni-like	0→1	–	–	–	–	240.0	4.886	160.0	4.876
Ni-like	0→1	–	–	–	–	1190.0	4.392	1110.0	4.404
Ni-like	0→1	2090.0	14.073	2010.0	26.064	–	–	–	–
Ni-like	0→1	2490.0	13.519	2410.0	25.048	1240.0	4.371	1160.0	4.380
Ni-like	0→1	–	–	–	–	2240.0	3.988	2160.0	4.015
Ni-like	0→1	7490.0	9.688	7410.0	17.392	–	–	–	–
Cu-like	Photon energy (eV)	2501.60		2592.99		3357.84		3445.64	
Cu-like	1/2→3/2	98.4	12.533	7.0	21.576	–	–	–	–
Cu-like	1/2→3/2	498.4	11.679	407.0	20.013	–	–	–	–
Cu-like	1/2→3/2	1048.4	10.796	957.0	18.386	191.5	1.570	104.4	2.785
Cu-like	1/2→3/2	1098.4	10.724	1007.0	18.261	241.5	1.560	154.4	2.768
Cu-like	1/2→3/2	2048.4	9.619	1957.0	16.221	1191.5	1.415	1104.4	2.497
Cu-like	1/2→3/2	2098.4	9.565	2007.0	16.126	1241.5	1.409	1154.4	2.487
Cu-like	1/2→3/2	3098.4	8.737	3007.0	14.621	2241.5	1.296	2154.4	2.274
Cu-like	1/2→3/2	6698.4	6.908	6607.0	11.334	5841.5	1.042	5754.4	1.795
Zn-like	Photon energy (eV)	2487.10		2577.50		3429.80		3343.30	
Zn-like	0→1	972.5	16.228	972.5	27.580	120.2	4.728	206.7	4.758
Zn-like	0→1	1022.5	16.120	1022.5	27.386	170.2	4.704	256.7	4.731
Zn-like	0→1	1972.5	14.483	1972.5	24.358	1120.2	4.261	1206.7	4.300
Zn-like	0→1	2022.5	14.411	2022.5	24.220	1170.2	4.240	1256.7	4.281
Zn-like	0→1	3022.5	13.186	3022.5	21.998	2170.2	3.887	2256.7	3.942
Zn-like	0→1	6622.5	10.442	6622.5	17.077	5770.2	3.078	5856.7	3.177

Fig. 3. Experimentally determined collisional excitation cross-sections for the 3d→4f and 3d→5f excitation in Ni-like Au and comparisons to HULLAC, FAC, and DWS calculations.

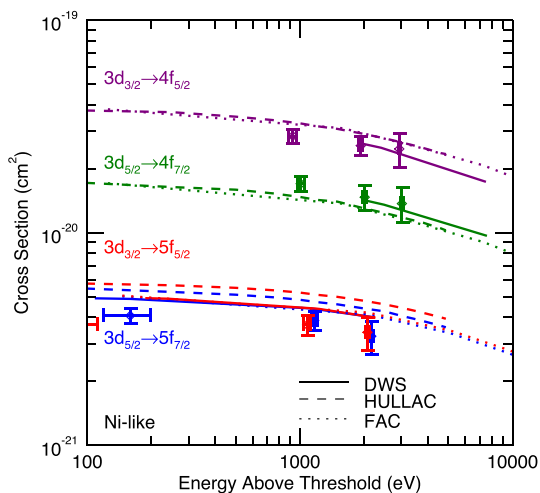
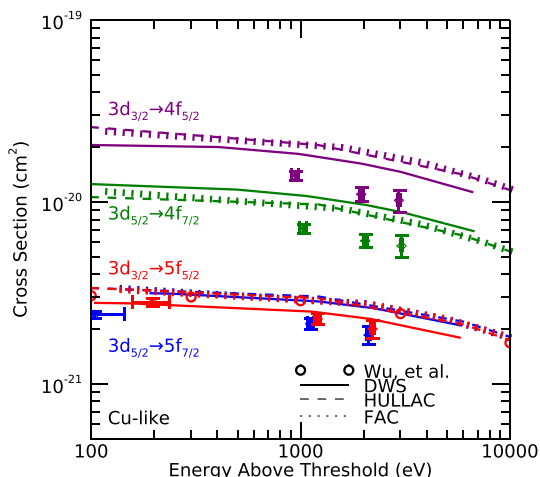


Fig. 4. Experimentally determined collisional excitation cross-sections for the 3d→4f and 3d→5f excitation in Cu-like Au and comparisons to HULLAC, FAC, and DWS calculations. A comparison with values from Wu *et al.* is also given.



a thermal (perpendicular) motion of the electrons can be ignored [37].

For line emission, the angular distribution resulting from the polarization, G_{CE} , can be expressed as $G_{CE} = 3/(3-P)$ for a dipole transition viewed at 90° . The angular distribution is defined as the ratio of the photon intensity at a given angle to that of the photon intensity at 0° [35]. The G_{CE} factors for each of the transitions were determined from the calculated polarizations. The angular distributions for the $4f \rightarrow 3d$ and $5f \rightarrow 3d$ Cu-like (Au^{51+}) and Zn-like (Au^{50+}) transitions are given in Figs. 10 and 11, respectively, as a function of energy above threshold, E_T . The G_{CE} values are 5% to 15% larger than unity and represent a necessary correction for the cross-section measurements. The differences between the DWS and FAC values for a given transition are less than $\sim 1\%$ and are an estimate on the uncertainty of each angular distribution fac-

Fig. 5. Experimentally determined collisional excitation cross-sections for the 3d→4f and 3d→5f excitation in Zn-like Au and comparisons to HULLAC, FAC, and DWS calculations.

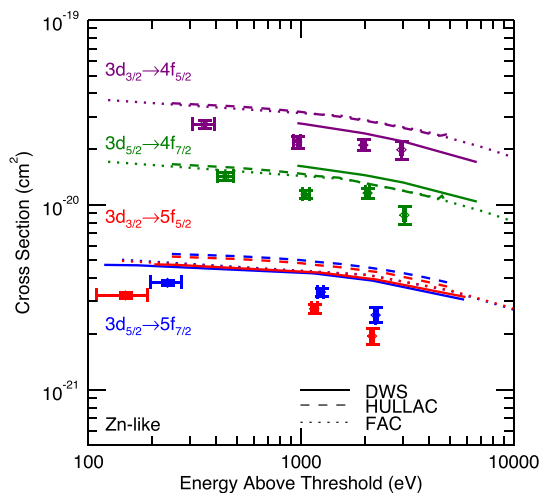


Fig. 6. Experimentally determined collisional excitation cross-sections for the 3d→4f and 3d→5f excitation in Ga-like Au and comparisons to HULLAC, FAC, and DWS calculations.

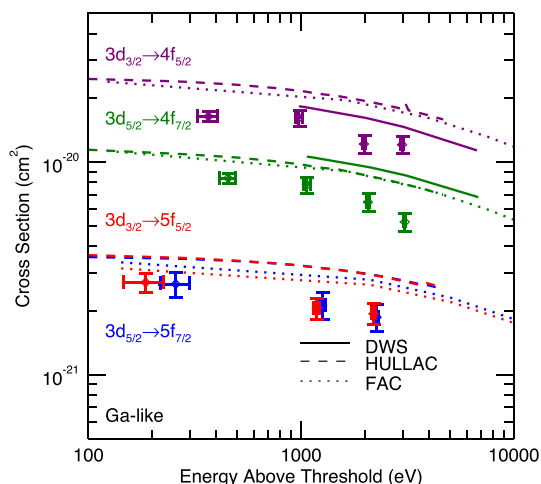


Fig. 7. Experimentally determined collisional excitation cross-sections for the 3d→4f and 3d→5f excitation in Ge-like Au and comparisons to HULLAC and FAC calculations.

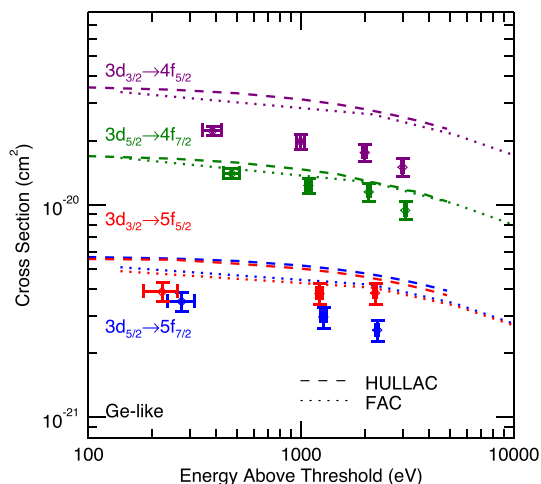


Fig. 8. Photon polarizations derived from DWS and FAC calculations as a function of energy above threshold, E_T , for the $4f \rightarrow 3d$ and $5f \rightarrow 3d$ Cu-like (Au^{50+}) transitions. A comparison with Wu *et al.* is also given.

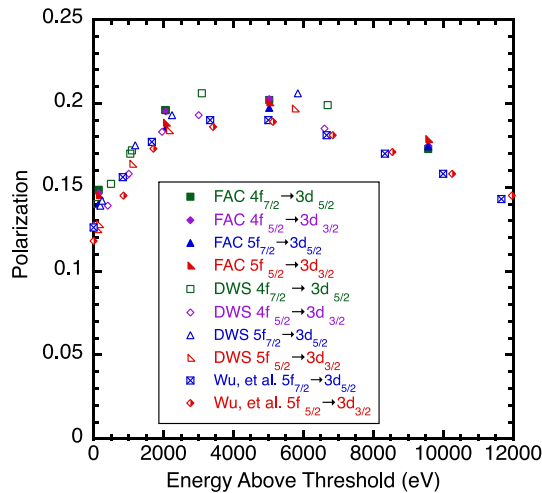


Fig. 9. Photon polarizations derived from DWS and FAC calculations as a function of energy above threshold, E_T , for the $4f \rightarrow 3d$ ($J = 1 \rightarrow 0$) and $5f \rightarrow 3d$ ($J = 1 \rightarrow 0$) Zn-like (Au^{49+}) transitions.

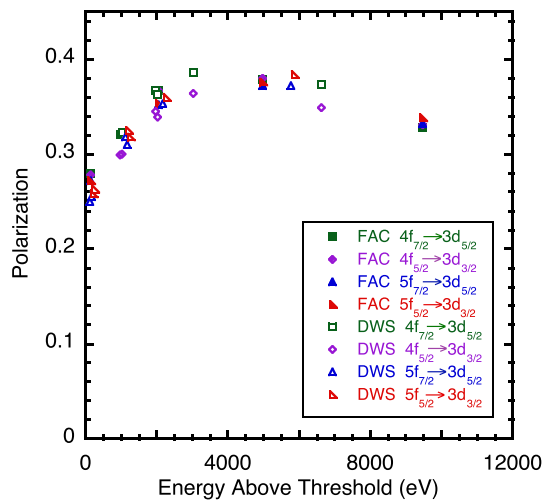


Fig. 10. Angular distributions derived from DWS and FAC photon polarization calculations as a function of energy above threshold, E_T , for the $4f \rightarrow 3d$ and $5f \rightarrow 3d$ Cu-like (Au^{50+}) transitions.

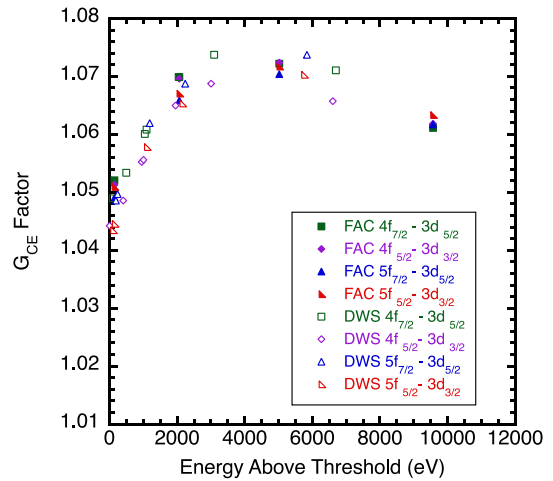
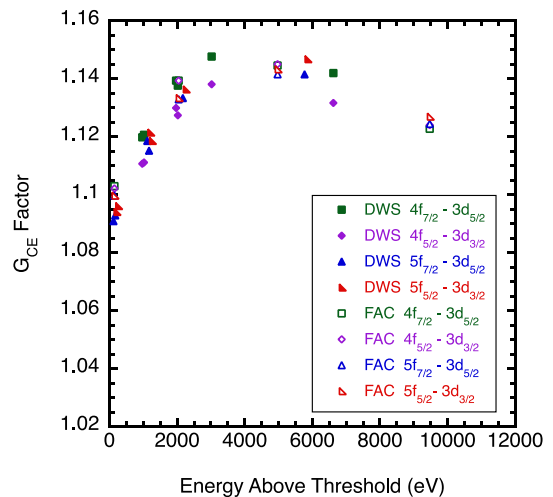


Fig. 11. Angular distributions derived from DWS and FAC photon polarization calculations as a function of energy above threshold, E_T , for the $4f \rightarrow 3d$ ($J = 1 \rightarrow 0$) and $5f \rightarrow 3d$ ($J = 1 \rightarrow 0$) Zn-like (Au^{49+}) transitions.



tor. This difference is not significant and is not included in the uncertainty estimates in the cross-section determinations.

5. Auger and electron cascade processes

The upper states for the $5f \rightarrow 3d$ transitions exist at an energy above the ionization potential for Cu-, Zn-, Ga-, and Ge-like Au ions. The upper state energies and ionization potentials are given in Table 7. One might expect the Auger process to affect the strength of these radiative decays. The $5f$ excited state will decay either through the emitting of an electron into the continuum or through radiative decay to the ground state of the original ion. The apparent experimentally determined cross-section from the line strength would

appear smaller without a correction for the fraction of the excited electrons lost through the Auger processes. The upper states for the $4f \rightarrow 3d$ transitions are below the ionization potential for these ions and should not be affected by Auger processes.

For each of the Ni- through Ge-like $5f \rightarrow 3d$ transitions, the collisional radiative model, SCRAM [38], was used to estimate the magnitude of the Auger processes and the branching ratios for the radiative decay. The branching ratio is the radiative decay rate from the excited level, i , to the ground level, l , divided by the sum over the radiative decay rates from level, i , to the levels in the same charge state, j , plus the sum over the Auger transitions from state, i , to levels in the next higher

Table 7. Branching ratios for radiative decay for select 5f→3d transitions.

Isonuclear sequence	Ionization potential (eV) [NIST]	5f _{5/2} →3d _{3/2}		5f _{7/2} →3d _{5/2}	
		Upper state energy (eV)	Radiative decay branching ratio	Upper state energy (eV)	Radiative decay branching ratio
Ni	4888	3458.3	1.000	3370.6	1.000
Cu	2941	3420.8	0.82 ± 0.01	3334.7	0.83 ± 0.01
Zn	2870	3382.7	0.79 ± 0.04	3296.6	0.79 ± 0.04
Ga	2708	3348.3	0.71 ± 0.03	3259.9	0.79 ± 0.07
Ge	2640	3312.2	0.71 ± 0.04	3226.5	0.75 ± 0.04

charge state, *k*. This can be expressed as follows:

$$\beta_{i,l} = \frac{A_{i,l}}{\sum_j^{RadDecay} A_{i,j} + \sum_k^{Auger} A_{i,k}} \quad (5)$$

The most significant contribution to the $\sum_j^{RadDecay} A_{i,j}$ term is $A_{i,l}$ at EBIT plasma conditions. The branching ratios are summarized in Table 7 for the Ni- to Ge-like Au iso-sequences. The Auger decay channels for the 5f excited states were found to be significant for the Cu-, Zn-, Ga-, and Ge-like Au ions and were corrected for in the determination of the 3d→5f collisional excitation cross-sections. As expected, the branching ratios for the 4f→3d excited states were found to be all greater than 0.99 for decays back to the ground state.

These complex ions have a lot of transitions so accounting for all the channels is a daunting task. The upper states are assumed to be primarily populated from direct collisional excitation rather than ionization, radiative cascades, or dielectronic capture in these low-density plasmas. Model completeness can introduce uncertainties in the branching ratio. Estimates of these uncertainties are given in the table. The branching ratio uncertainties have been included in the total error for the presented cross-sections.

In addition, electrons excited into higher energy levels that decay or cascade into the upper levels of the transitions under study could affect the cross-section measurements. These cascading electrons would tend to increase the population of the upper level of a transition and increase the measured line emission. The experimentally inferred cross-section would appear to be enhanced from this additional electron population channel. At these low densities, this effect should be small. From the SCRAM modeling, the strong transitions into the upper states of the transitions under study were identified. The branching ratios for these cascading transitions were used to estimate the fraction of the upper-level populations from cascades. We estimate that the total contribution to the electron populations from cascading electrons was at most 1%–2%. The enhancement in the emission of each measured transition is small and well within the uncertainty of each cross-section measurement.

6. Discussion

The comparisons between the total calculated cross-section from HULLAC, FAC, and DWS, and the experimentally determined cross-sections for the 3d→4f and 3d→5f excitations are given in Fig. 3 for Ni-like, Fig. 4 for Cu-like, Fig. 5 for Zn-like, Fig. 6 for Ga-like, and Fig. 7 for Ge-like Au. The points with uncertainties are the experimentally determined cross-sections. As stated above, the lines are the values from the calculations. The experimentally determined cross-sections and uncertainties are summarized in Tables 8, 9, 10, 11, and 12 for Ni-, Cu-, Zn-, Ga- and Ge-like gold respectively. The uncertainties on each point included the statistical error from the counts in the spectral line and RR features, the uncertainty in the fits to the line or RR features in each charge state, the uncertainties in the Auger processes, and the uncertainty in the XRS photometric calibrations. Typical percentage values for each type of uncertainty for an individual experimental cross-section are given in Table 13. The largest source of uncertainty in these measurements is the fitting error of the RR peaks. All these uncertainties are all added in quadrature. The uncertainty on a value given in the cross-section tables will be less since several measurements and associate error were averaged together.

For Ni-like and Cu-like Au, the cross-sections have been experimentally determined at approximately 1, 2, and 3 keV above E_T for the 3d→4f excitations ($E_T \sim 2.5$ keV) and at approximately 0.1, 1, and 2 keV above E_T for the 3d→5f excitations ($E_T \sim 3.3$ keV). The 3d→4f and 3d→5f experimentally determined cross-sections are in reasonable agreement with the calculations for Ni-like Au. For Cu-like gold the 3d→5f experimentally determined cross-sections are in reasonable agreement with the calculations; however, the 3d→4f experimentally determined cross-sections are about 30% smaller than those from the calculations.

For Zn-like, Ga-like, and Ge-like Au ions, the cross-sections for both the 3d→4f and 3d→5f excitations have been experimentally determined at similar energies above E_T as stated for the Ni-like and Cu-like Au ions. Additionally, for the 3d→4f transitions, experimentally inferred cross-sections were determined ~0.4 keV above E_T for the Zn-like, Ga-like, and Ge-like Au ions. Both the Zn-like and Ga-like experimentally determined 3d→4f and 3d→5f cross-sections are in fair agreement but about 25% less than the cal-

Table 8. Summary of experimentally determined collisional excitation cross-sections for $3d_{3/2} \rightarrow 4f_{5/2}$, $3d_{5/2} \rightarrow 4f_{7/2}$, $3d_{3/2} \rightarrow 5f_{5/2}$, and $3d_{5/2} \rightarrow 5f_{7/2}$ in Ni-like Au.

Transition	Measured photon energy (eV)	Energy above threshold (eV)	Cross-section (cm ²)
$3d_{5/2} \rightarrow 5f_{7/2}$	3370.6	159 ± 40	$4.06 \pm 0.31 \times 10^{-21}$
$3d_{5/2} \rightarrow 5f_{7/2}$	3370.6	1169 ± 40	$3.85 \pm 0.40 \times 10^{-21}$
$3d_{5/2} \rightarrow 5f_{7/2}$	3370.6	2169 ± 40	$3.25 \pm 0.58 \times 10^{-21}$
$3d_{3/2} \rightarrow 5f_{5/2}$	3458.3	71 ± 40	$3.70 \pm 0.28 \times 10^{-21}$
$3d_{3/2} \rightarrow 5f_{5/2}$	3458.3	1081 ± 40	$3.67 \pm 0.39 \times 10^{-21}$
$3d_{3/2} \rightarrow 5f_{5/2}$	3458.3	2081 ± 40	$3.39 \pm 0.60 \times 10^{-21}$
$3d_{5/2} \rightarrow 4f_{7/2}$	2519.8	1010 ± 40	$1.69 \pm 0.13 \times 10^{-20}$
$3d_{5/2} \rightarrow 4f_{7/2}$	2519.8	2020 ± 40	$1.46 \pm 0.20 \times 10^{-20}$
$3d_{5/2} \rightarrow 4f_{7/2}$	2519.8	3020 ± 40	$1.36 \pm 0.26 \times 10^{-20}$
$3d_{3/2} \rightarrow 4f_{5/2}$	2603.6	926 ± 40	$2.84 \pm 0.22 \times 10^{-20}$
$3d_{3/2} \rightarrow 4f_{5/2}$	2603.6	1936 ± 40	$2.56 \pm 0.27 \times 10^{-20}$
$3d_{3/2} \rightarrow 4f_{5/2}$	2603.6	2936 ± 40	$2.47 \pm 0.45 \times 10^{-20}$

Table 9. Summary of experimentally determined collisional excitation cross-sections for $3d_{3/2} \rightarrow 4f_{5/2}$, $3d_{5/2} \rightarrow 4f_{7/2}$, $3d_{3/2} \rightarrow 5f_{5/2}$, and $3d_{5/2} \rightarrow 5f_{7/2}$ ($J = 1/2 \rightarrow 3/2$) in Cu-like Au.

Transition	Measured photon energy (eV)	Energy above threshold (eV)	Cross-section (cm ²)
$3d_{5/2} \rightarrow 5f_{7/2}$	3334.7	103 ± 40	$2.39 \pm 0.11 \times 10^{-21}$
$3d_{5/2} \rightarrow 5f_{7/2}$	3334.7	1113 ± 40	$2.13 \pm 0.14 \times 10^{-21}$
$3d_{5/2} \rightarrow 5f_{7/2}$	3334.7	2113 ± 40	$1.85 \pm 0.21 \times 10^{-21}$
$3d_{3/2} \rightarrow 5f_{5/2}$	3420.8	196 ± 40	$2.80 \pm 0.14 \times 10^{-21}$
$3d_{3/2} \rightarrow 5f_{5/2}$	3420.8	1206 ± 40	$2.26 \pm 0.16 \times 10^{-21}$
$3d_{3/2} \rightarrow 5f_{5/2}$	3420.8	2206 ± 40	$2.00 \pm 0.23 \times 10^{-21}$
$3d_{5/2} \rightarrow 4f_{7/2}$	2501.9	940 ± 40	$1.39 \pm 0.083 \times 10^{-20}$
$3d_{5/2} \rightarrow 4f_{7/2}$	2501.9	1950 ± 40	$1.10 \pm 0.092 \times 10^{-20}$
$3d_{5/2} \rightarrow 4f_{7/2}$	2501.9	2950 ± 40	$1.01 \pm 0.14 \times 10^{-20}$
$3d_{3/2} \rightarrow 4f_{5/2}$	2589.4	1028 ± 40	$7.11 \pm 0.43 \times 10^{-21}$
$3d_{3/2} \rightarrow 4f_{5/2}$	2589.4	2038 ± 40	$6.10 \pm 0.51 \times 10^{-21}$
$3d_{3/2} \rightarrow 4f_{5/2}$	2589.4	3038 ± 40	$5.72 \pm 0.80 \times 10^{-21}$

culations. Finally, the Ge-like Au experimentally determined cross-sections are also about 25% below the calculations. However, the experimentally determined cross-sections for the $3d_{3/2} \rightarrow 4f_{5/2}$ transition are about 50% below the calculations. These measurements demonstrate that some errors are likely to exist in the calculations of excitation cross-sections. It is also possible that the theoretical Auger or radiative rates contribute to the discrepancies.

The majority of the experimentally inferred cross-sections are less than theory predicts. A hohlraum simulation using calculated cross-sections that are too large might over-predict the emission from these M-shell transitions by ~30%. This should be observable in a discrepancy between predicted energetics and radiation drive from a hohlraum target and experimental measurements. Recent View Factor experiments in hohlraums on the NIF have provided the first X-ray drive measurements from the capsule

point of view [39]. The experiments show a 15%–25% deficit in the X-ray drive on the target relative to simulations. The non-thermal gold M-shell emission is a significant contribution to the radiation drive on the capsule in these conditions. The use of incorrect cross-sections for these M-shell lines in the hohlraum modeling could account for and explain at least part of this drive discrepancy.

7. Conclusion

The experimentally determined cross-sections have been determined for the $3d_{5/2} \rightarrow 5f_{7/2}$, $3d_{3/2} \rightarrow 5f_{5/2}$, $3d_{5/2} \rightarrow 4f_{7/2}$, and $3d_{3/2} \rightarrow 4f_{5/2}$ excitations in Ni-, Cu-, Zn-, Ga- and Ge-like gold ions. These cross-sections have been determined at a few hundred eVs to approximately 3 keV above the threshold energy for the excitations. For these measurements, the LLNL EBIT-I was used to create gold plasmas having single

Table 10. Summary of experimentally determined collisional excitation cross-sections for $3d_{3/2} \rightarrow 4f_{5/2}$, $3d_{5/2} \rightarrow 4f_{7/2}$, $3d_{3/2} \rightarrow 5f_{5/2}$, and $3d_{5/2} \rightarrow 5f_{7/2}$ in Zn-like Au.

Transition	Measured photon energy (eV)	Energy above threshold (eV)	Cross Section (cm ²)
$3d_{5/2} \rightarrow 5f_{7/2}$	3296.6	235 ± 40	$3.78 \pm 0.13 \times 10^{-21}$
$3d_{5/2} \rightarrow 5f_{7/2}$	3296.6	1240 ± 40	$3.36 \pm 0.17 \times 10^{-21}$
$3d_{5/2} \rightarrow 5f_{7/2}$	3296.6	2244 ± 40	$2.53 \pm 0.24 \times 10^{-21}$
$3d_{3/2} \rightarrow 5f_{5/2}$	3382.7	149 ± 40	$3.23 \pm 0.13 \times 10^{-21}$
$3d_{3/2} \rightarrow 5f_{5/2}$	3382.7	1154 ± 40	$2.73 \pm 0.14 \times 10^{-21}$
$3d_{3/2} \rightarrow 5f_{5/2}$	3382.7	2158 ± 40	$1.94 \pm 0.20 \times 10^{-21}$
$3d_{5/2} \rightarrow 4f_{7/2}$	2480.2	442 ± 40	$1.42 \pm 0.078 \times 10^{-20}$
$3d_{5/2} \rightarrow 4f_{7/2}$	2480.2	1051 ± 40	$1.13 \pm 0.057 \times 10^{-20}$
$3d_{5/2} \rightarrow 4f_{7/2}$	2480.2	2057 ± 40	$1.15 \pm 0.073 \times 10^{-20}$
$3d_{5/2} \rightarrow 4f_{7/2}$	2480.2	3061 ± 40	$8.79 \pm 0.99 \times 10^{-21}$
$3d_{3/2} \rightarrow 4f_{5/2}$	2572.8	350 ± 40	$2.72 \pm 0.15 \times 10^{-20}$
$3d_{3/2} \rightarrow 4f_{5/2}$	2572.8	959 ± 40	$2.18 \pm 0.17 \times 10^{-20}$
$3d_{3/2} \rightarrow 4f_{5/2}$	2572.8	1964 ± 40	$2.10 \pm 0.14 \times 10^{-20}$
$3d_{3/2} \rightarrow 4f_{5/2}$	2572.8	2968 ± 40	$1.98 \pm 0.22 \times 10^{-20}$

Table 11. Summary of experimentally determined collisional excitation cross-sections for $3d_{3/2} \rightarrow 4f_{5/2}$, $3d_{5/2} \rightarrow 4f_{7/2}$, $3d_{3/2} \rightarrow 5f_{5/2}$, and $3d_{5/2} \rightarrow 5f_{7/2}$ ($J = 1/2 \rightarrow 3/2$) in Ga-like Au.

Transition	Measured photon energy (eV)	Energy above threshold (eV)	Cross-section (cm ²)
$3d_{5/2} \rightarrow 5f_{7/2}$	3259.9	257 ± 40	$2.66 \pm 0.36 \times 10^{-21}$
$3d_{5/2} \rightarrow 5f_{7/2}$	3259.9	1257 ± 40	$2.11 \pm 0.30 \times 10^{-21}$
$3d_{5/2} \rightarrow 5f_{7/2}$	3259.9	2266 ± 40	$1.85 \pm 0.27 \times 10^{-21}$
$3d_{3/2} \rightarrow 5f_{5/2}$	3348.3	185 ± 40	$2.71 \pm 0.28 \times 10^{-21}$
$3d_{3/2} \rightarrow 5f_{5/2}$	3348.3	1186 ± 40	$2.04 \pm 0.23 \times 10^{-21}$
$3d_{3/2} \rightarrow 5f_{5/2}$	3348.3	2194 ± 40	$1.93 \pm 0.22 \times 10^{-21}$
$3d_{5/2} \rightarrow 4f_{7/2}$	2469.1	453 ± 40	$8.37 \pm 0.43 \times 10^{-21}$
$3d_{5/2} \rightarrow 4f_{7/2}$	2469.1	1065 ± 40	$7.79 \pm 0.67 \times 10^{-21}$
$3d_{5/2} \rightarrow 4f_{7/2}$	2469.1	2065 ± 40	$6.46 \pm 0.62 \times 10^{-21}$
$3d_{5/2} \rightarrow 4f_{7/2}$	2469.1	3073 ± 40	$5.22 \pm 0.50 \times 10^{-21}$
$3d_{3/2} \rightarrow 4f_{5/2}$	2556.3	366 ± 40	$1.63 \pm 0.085 \times 10^{-20}$
$3d_{3/2} \rightarrow 4f_{5/2}$	2556.3	977 ± 40	$1.60 \pm 0.14 \times 10^{-20}$
$3d_{3/2} \rightarrow 4f_{5/2}$	2556.3	1978 ± 40	$1.21 \pm 0.11 \times 10^{-20}$
$3d_{3/2} \rightarrow 4f_{5/2}$	2556.3	2986 ± 40	$1.20 \pm 0.11 \times 10^{-20}$

and two-stepped monoenergetic beams with several different energies. The cross-sections were determined from fits to the measured photometrically calibrated spectra that contained collisionally excited line transitions and RR emission from these plasmas. The effects of polarization and Auger processes in the beam plasmas are accounted for in the experimentally inferred cross-section determination. Cross-sections calculated by available modeling codes (FAC, DWS, and HULLAC) do not adequately reproduce all of the measurements. In general, the disagreement between the experimentally inferred and calculated transitions were less than ~30%, but were found to be as high as 50% for some cross-sections.

8. Disclaimer

This document was prepared as an account of work sponsored by an agency of the United States government. Neither the United States government nor Lawrence Livermore National Security, LLC, nor any of their employees makes any warranty, expressed or implied, or assumes any legal liability or responsibility for the accuracy, completeness, or usefulness of any information, apparatus, product, or process disclosed, or represents that its use would not infringe privately owned rights. Reference herein to any specific commercial product, process, or service by trade name, trademark, manufacturer, or otherwise does not necessarily constitute or im-

Table 12. Summary of experimentally determined collisional excitation cross-sections for $3d_{3/2} \rightarrow 4f_{5/2}$, $3d_{5/2} \rightarrow 4f_{7/2}$, $3d_{3/2} \rightarrow 5f_{5/2}$, and $3d_{5/2} \rightarrow 5f_{7/2}$ in Ge-like Au.

Transition	Measured photon energy (eV)	Energy above threshold (eV)	Cross-section (cm ²)
$3d_{5/2} \rightarrow 5f_{7/2}$	3226.5	274 ± 40	$3.50 \pm 0.36 \times 10^{-21}$
$3d_{5/2} \rightarrow 5f_{7/2}$	3226.5	1274 ± 40	$2.96 \pm 0.34 \times 10^{-21}$
$3d_{5/2} \rightarrow 5f_{7/2}$	3226.5	2283 ± 40	$2.56 \pm 0.29 \times 10^{-21}$
$3d_{3/2} \rightarrow 5f_{5/2}$	3312.2	221 ± 40	$3.88 \pm 0.40 \times 10^{-21}$
$3d_{3/2} \rightarrow 5f_{5/2}$	3312.2	1222 ± 40	$3.81 \pm 0.43 \times 10^{-21}$
$3d_{3/2} \rightarrow 5f_{5/2}$	3312.2	2230 ± 40	$3.83 \pm 0.43 \times 10^{-21}$
$3d_{5/2} \rightarrow 4f_{7/2}$	2450.5	472 ± 40	$1.39 \pm 0.072 \times 10^{-20}$
$3d_{5/2} \rightarrow 4f_{7/2}$	2450.5	1083 ± 40	$1.22 \pm 0.10 \times 10^{-20}$
$3d_{5/2} \rightarrow 4f_{7/2}$	2450.5	2084 ± 40	$1.14 \pm 0.11 \times 10^{-20}$
$3d_{5/2} \rightarrow 4f_{7/2}$	2450.5	3092 ± 40	$9.38 \pm 0.89 \times 10^{-21}$
$3d_{3/2} \rightarrow 4f_{5/2}$	2539.9	383 ± 40	$2.21 \pm 0.11 \times 10^{-20}$
$3d_{3/2} \rightarrow 4f_{5/2}$	2539.9	994 ± 40	$1.97 \pm 0.16 \times 10^{-20}$
$3d_{3/2} \rightarrow 4f_{5/2}$	2539.9	1994 ± 40	$1.75 \pm 0.17 \times 10^{-20}$
$3d_{3/2} \rightarrow 4f_{5/2}$	2539.9	3003 ± 40	$1.49 \pm 0.14 \times 10^{-20}$

Table 13. Typical fractional uncertainties on an individual experimental cross-section.

Isonuclear sequence	28	29	30	31	32
Counts in the spectral line features	0.01	0.03	0.03	0.03	0.02
Counts in the RR features	0.02	0.08	0.06	0.04	0.04
RR fitting error	0.08	0.09	0.09	0.09	0.09
Auger processes	0.0	0.01	0.04	0.06	0.04
XRS calibration	0.05	0.05	0.05	0.05	0.05
Total error	0.11	0.14	0.13	0.13	0.12

ply its endorsement, recommendation, or favoring by the United States government or Lawrence Livermore National Security, LLC. The views and opinions of authors expressed herein do not necessarily state or reflect those of the United States government or Lawrence Livermore National Security, LLC, and shall not be used for advertising or product endorsement purposes.

Acknowledgments

This work was done under the auspices of the U.S. Department of Energy by Lawrence Livermore National Laboratory under Contract No. DE-AC52-07NA27344. Sandia National Laboratories is a multimission laboratory managed and operated by National Technology and Engineering Solutions of Sandia, LLC., a wholly owned subsidiary of Honeywell International, Inc., for the U.S. Department of Energy's National Nuclear Security Administration under Contract No. DE-NA-0003525.

Article information

History dates

Received: 23 April 2023

Accepted: 28 September 2023

Version of record online: 24 November 2023

Copyright

© 2023 The Author(s). Permission for reuse (free in most cases) can be obtained from [copyright.com](https://www.copyright.com).

Data availability

Data generated or analyzed during this study are provided in full within the published article.

Author information

Author ORCIDs

M.J. May <https://orcid.org/0000-0001-7967-7337>

S.B. Hansen <https://orcid.org/0000-0002-1886-9770>

Author notes

Peter Beiersdorfer served as an Associate Editor at the time of manuscript review and acceptance; peer review and editorial decisions regarding this manuscript were handled by another Editorial Board Member.

Author contributions

Data curation: MJM, SBH, JHS, KJR

Formal analysis: MJM, NMJ

Investigation: MJM, SBH

Resources: GVB, FSP, RLK, CAK, KRB

Supervision: PB

Writing – original draft: MJM

Writing – review & editing: SBH, PB, NMJ

Competing interests

The authors declare there are no competing interests.

References

1. K.L. Wong, P.T. Springer, J.H. Hammer, C.A. Iglesias, A.L. Osterheld, M.E. Foord, H.C. Bruns, and J.A. Emig. *Phys. Rev. Lett.* **80**, 2334 (1998). doi:[10.1103/PhysRevLett.80.2334](https://doi.org/10.1103/PhysRevLett.80.2334).
2. A.L. Velikovich, J. Davis, V.I. Oreshkin, J.P. Apruzese, R.Q. Clark, J.W. Thornhill, and L.I. Rudakov. *Phys. Plasmas*, **8**, 4509 (2001). doi:[10.1063/1.1398572](https://doi.org/10.1063/1.1398572).
3. C. De Michelis and M. Mattioli. *Rep. Prog. Phys.* **47**, 1233 (1984). doi:[10.1088/0034-4885/47/10/001](https://doi.org/10.1088/0034-4885/47/10/001).
4. J.E. Rice, J.L. Terry, K.B. Fournier, M.A. Graf, M. Finkenthal, M.J. May, E.S. Marmor, W.H. Goldstein, and A.E. Hubbard. *J. Phys. B: At. Mol. Opt. Phys.* **29**, 2191–2208(1996). doi:[10.1088/0953-4075/29/11/011](https://doi.org/10.1088/0953-4075/29/11/011).
5. P. Buratti, E. Barbato, and G. Bracco, et al. *Phys. Rev. Lett.* **82**(3), 560–563(1999). doi:[10.1103/PhysRevLett.82.560](https://doi.org/10.1103/PhysRevLett.82.560).
6. J.C. Raymond and N.C. Brickhouse. *Astrophys. Space Sci.* **237**, 321 (1996). doi:[10.1007/BF02424437](https://doi.org/10.1007/BF02424437).
7. H.R. Griem. *Phys. Fluids B*, **4**, 2346 (1992). doi:[10.1063/1.860205](https://doi.org/10.1063/1.860205).
8. M. Fajardo, P. Audebert, P. Renaudin, H. Yashiro, R. Shepherd, J.-C. Gauthier, and C. Chenais-Popovics. *Phys. Rev. Lett.* **86**, 1231 (2001). doi:[10.1103/PhysRevLett.86.1231](https://doi.org/10.1103/PhysRevLett.86.1231).
9. C.Y. Côté, J.C. Kieffer, and O. Peyrusse. *Phys. Rev. E*, **56**, 992 (1997). doi:[10.1103/PhysRevE.56.992](https://doi.org/10.1103/PhysRevE.56.992).
10. S.W. Haan, J.D. Lindl, and D.A. Callahan, et al. *Phys. Plasmas*, **18**, 051001 (2011). doi:[10.1063/1.3592169](https://doi.org/10.1063/1.3592169).
11. J.D. Lindl, P. Amendt, R.L. Berger, S.G. Glendinning, S.H. Glenzer, S.W. Haan, R.L. Kauffman, O.L. Landen, and L.J. Suter. *Phys. Plasmas*, **11**, 339 (2004). doi:[10.1063/1.1578638](https://doi.org/10.1063/1.1578638).
12. D.E. Hinkel, M.J. Edwards, and P.A. Amendt, et al. *Plasma Phys. Contr. F.* **55**(12), (2013). doi:[10.1088/0741-3335/55/12/124015](https://doi.org/10.1088/0741-3335/55/12/124015).
13. C. Cerjan, P.T. Springer, and S.M. Sepke. *Phys. Plasmas*, **20**, 056319 (2013). doi:[10.1063/1.4802196](https://doi.org/10.1063/1.4802196).
14. R.E. Marrs, K. Widmann, G.V. Brown, R.F. Heeter, S.A. MacLaren, M.J. May, A.S. Moore, and M.B. Schneider. *Rev. Sci. Instrum.* **86**, 103511 (2015). doi:[10.1063/1.4934542](https://doi.org/10.1063/1.4934542).
15. P. Beiersdorfer, M.J. May, J.H. Scofield, and S.B. Hansen. *High Energ. Dens. Phys.* **8**, 271 (2012). doi:[10.1016/j.hedp.2012.03.003](https://doi.org/10.1016/j.hedp.2012.03.003).
16. R. Marrs, P. Beiersdorfer, and D. Schneider, et al. *Phys. Today*, **47**, 27 (1994). doi:[10.1063/1.881419](https://doi.org/10.1063/1.881419).
17. M.A. Levine, R.E. Marrs, J.R. Henderson, D.A. Knapp, and M.B. Schneider. *Phys. Scripta*, **22**, 157 (1988). doi:[10.1088/0031-8949/1988/T22/024](https://doi.org/10.1088/0031-8949/1988/T22/024).
18. H. Chen and P. Beiersdorfer. *Can. J. Phys.* **86**, 55 (2008). doi:[10.1139/p07-152](https://doi.org/10.1139/p07-152).
19. A. Bar-Shalom, M. Klapisch, and J. Oreg. *J. Quant. Spectrosc. Radiat. Transfer*, **71**, 169 (2001). doi:[10.1016/S0022-4073\(01\)00066-8](https://doi.org/10.1016/S0022-4073(01)00066-8).
20. H.L. Zhang, D.H. Sampson, and R.E.H. Clark. *Phys. Rev. A*, **41**, 198 (1990). doi:[10.1103/PhysRevA.41.198](https://doi.org/10.1103/PhysRevA.41.198).
21. M.F. Gu. In *Proceedings of the 14th APS topical conference on atomic processes in plasmas. Edited by J.S. Cohen, S. Mazevet, and D.P. Kilcrease. AIP Conf. Proc. No. 730 AIP, New York. 2004. p. 127.* doi:[10.1063/1.1824864](https://doi.org/10.1063/1.1824864).
22. M.F. Gu. *Can. J. Phys.* **86**(1), 351 (2008). doi:[10.1139/p07-105](https://doi.org/10.1139/p07-105).
23. F.S. Porter, M.D. Audley, and P. Beiersdorfer, et al. *Proc. SPIE*, **4140**, 407–418(2000). doi:[10.1117/12.409137](https://doi.org/10.1117/12.409137).
24. F.S. Porter, G.V. Brown, and K.R. Boyce, et al. *Rev. Sci. Instr.* **75**, 3772 (2004). doi:[10.1063/1.1781758](https://doi.org/10.1063/1.1781758).
25. H. Chen, P. Beiersdorfer, and J.H. Scofield, et al. *Astrophys. J. Lett.* **567**(2), L169–L172(2002). doi:[10.1086/340007](https://doi.org/10.1086/340007).
26. H. Chen, P. Beiersdorfer, and J.H. Scofield, et al. *Astrophys. J.* **618**(2), 1086–1094(2005). doi:[10.1086/426135](https://doi.org/10.1086/426135).
27. M.J. May, K.B. Fournier, P. Beiersdorfer, H. Chen, and K.L. Wong. *Phys. Rev. E*. **68**, 036402 (2003). doi:[10.1103/PhysRevE.68.036402](https://doi.org/10.1103/PhysRevE.68.036402).
28. M.J. May, S.B. Hansen, J. Scofield, M. Schneider, K. Wong, and P. Beiersdorfer. *Phys. Rev. E*. **84**, 046402 (2011). doi:[10.1103/PhysRevE.84.046402](https://doi.org/10.1103/PhysRevE.84.046402).
29. M.J. May, P. Beiersdorfer, and N. Jordan, et al. *AIP Conf. Proc.* **1811**, 190009 (2017). doi:[10.1063/1.4975752](https://doi.org/10.1063/1.4975752).
30. M.J. May, P. Beiersdorfer, and M. Schneider, et al. *AIP Conf. Proc.* **730**, 61 (2004). doi:[10.1063/1.1824857](https://doi.org/10.1063/1.1824857).
31. Z.W. Wu, C.Z. Dong, and J. Jiang. *Phys. Rev. A*, **86**, 022712 (2012). doi:[10.1103/PhysRevA.86.022712](https://doi.org/10.1103/PhysRevA.86.022712).
32. P. Beiersdorfer, J. Crespo López-Urrutia, V. Decaux, K. Widmann, and P. Neill. *Rev. Sci. Instrum.* **68**(1), 1073–1076(1997). doi:[10.1063/1.1148222](https://doi.org/10.1063/1.1148222).
33. F.A. Parpia, C. Froese Fischera, and P. Grant. *Comput. Phys. Commun.* **94**, 249 (1996). doi:[10.1016/0010-4655\(95\)00136-0](https://doi.org/10.1016/0010-4655(95)00136-0).
34. J.H. Scofield. *Phys. Rev. A*, **40**(3), 3054 (1989). doi:[10.1103/PhysRevA.40.3054](https://doi.org/10.1103/PhysRevA.40.3054).
35. I.C. Percival and M.J. Seaton. *Philos. Trans. R. Soc. Lond. Ser. A*, **251**, 113 (1958). doi:[10.1098/rsta.1958.0011](https://doi.org/10.1098/rsta.1958.0011).
36. P. Beiersdorfer, D.A. Vogel, and K.J. Reed, et al. *Phys. Rev. A*, **53**(6), 3974–3981(1996). doi:[10.1103/PhysRevA.53.3974](https://doi.org/10.1103/PhysRevA.53.3974).
37. M.F. Gu, D.W. Savin, and P. Beiersdorfer. *J. Phys. B*, **32**, 5371 (1999). doi:[10.1103/PhysRevA.53.3974](https://doi.org/10.1103/PhysRevA.53.3974).
38. H.A. Scott and S.B. Hansen. *High Energ. Dens. Phys.* **6**, 39 (2010). doi:[10.1016/j.hedp.2009.07.003](https://doi.org/10.1016/j.hedp.2009.07.003).
39. S.A. MacLaren, M.B. Schneider, and K. Widmann, et al. *Phys. Rev. Lett.* **112**, 105003 (2014). doi:[10.1103/PhysRevLett.112.105003](https://doi.org/10.1103/PhysRevLett.112.105003).